On the accuracy of internal wave generation method in a non-hydrostatic wave model to generate and absorb dispersive and directional waves

Vasarmidis, Panagiotis; Stratigaki, Vasiliki; Suzuki, Tomohiro; Zijlema, Marcel; Troch, Peter

DOI
10.1016/j.oceaneng.2020.108303

Publication date
2021

Document Version
Final published version

Published in
Ocean Engineering

Ocean Engineering 219 (2021) 108303

Contents lists available at ScienceDirect

Ocean Engineering

journal homepage: www.elsevier.com/locate/oceaneng

On the accuracy of internal wave generation method in a non-hydrostatic wave model to generate and absorb dispersive and directional waves

Panagiotis Vasarmidis [a,*], Vasiliki Stratigaki [a], Tomohiro Suzuki [b,c], Marcel Zijlema [c], Peter Troch [a]

[a] Ghent University, Department of Civil Engineering, Technologiepark 60, 9052, Ghent, Belgium
[b] Flanders Hydraulics Research, Berchemlei 115, 2140, Antwerp, Belgium
[c] Delft University of Technology, Department of Hydraulic Engineering, Stevinweg 1, 2628, CN, Delft, the Netherlands

ARTICLE INFO

Keywords:
Non-hydrostatic wave model
SWASH
Internal wave generation
Weakly reflective wave generation
Short-crested waves

ABSTRACT

The weakly reflective wave generation is a wave generation and absorption method in phase-resolving models, based on the assumption that the waves propagating towards the wave generation boundary are small amplitude shallow water waves with direction perpendicular to the boundary. This assumption makes the method weakly reflective for dispersive and directional waves. The internal wave generation method was proposed by Vasarmidis et al. (2019b) as an alternative, for the non-hydrostatic wave model, SWASH, to avoid reflections. In this study, a comparison is made between the performance of the new internal wave generation method and the weakly reflective wave generation method. It is shown that using the internal wave generation leads to a significantly more accurate prediction of the resulting wave field in case of waves reflected back to the numerical boundary. Additionally, the internal wave generation method is extended to short-crested waves and SWASH is validated for the first time with experimental data for the cases of wave propagation over a shoal and wave diffraction around a wall. The proposed extended internal wave generation method increases the capability of SWASH towards the study of wave propagation of highly dispersive short-crested waves in coastal environments with minimal reflection from the boundaries.

1. Introduction

One of the challenges that the engineering world has to face is the study of coastal environments, in order to assess their vulnerability due to the climate change and the resulting increase of the wave heights. Numerical models are used more and more often in order to get a realistic and accurate representation of the waves in the field and their transformation over time and space. Several numerical models are based on the Reynolds-Averaged Navier-Stokes equations (e.g. Higuera et al., 2013a; Lin and Liu, 1998), which are able to resolve wave propagation and breaking processes and to provide three-dimensional velocity and pressure profiles, but at the same time add the restriction of very high computational cost. As an alternative, numerical models have been developed that are using approximated equations, typically averaged over the depth. Such models are necessary tools, especially when long duration sea states and large domains are considered.

Boussinesq-type wave models are frequently used to study wave transformation in coastal regions. Such models constitute the depth-integrated equations of surface wave propagation and include perturbation expansions in order to improve their wave dispersion and nonlinear dynamics (e.g. Lynett and Liu, 2002; Shi et al., 2012; Sørensen et al., 2004). In addition, high-order Boussinesq-type models have been developed to further improve the nonlinear effects, either through the use of higher order polynomial approximations for the vertical distribution of the flow field (Gobbi et al., 2000) or by means of the multi-layer concept of Lynett and Liu (2004). Typically, Boussinesq-type wave models are highly complicated due to e.g. high-order spatial derivatives and thus computationally expensive.

An alternative to the Boussinesq-type wave models are the non-hydrostatic wave models (e.g. Bai and Cheung, 2012; Ma et al., 2012; Stelling and Zijlema, 2003) which constitute a robust tool, able to accurately describe coastal phenomena. Non-hydrostatic wave models can directly resolve the vertical and horizontal flow structure by retaining the 3D momentum equations and can improve their wave

* Corresponding author.
E-mail addresses: panagiotis.vasarmidis@ugent.be (P. Vasarmidis), vicky.stratigaki@ugent.be (V. Stratigaki), tomohiro.suzuki@mow.vlaanderen.be (T. Suzuki), m.zijlema@tudelft.nl (M. Zijlema), peter.troch@ugent.be (P. Troch).

https://doi.org/10.1016/j.oceaneng.2020.108303
Received 17 July 2020; Received in revised form 22 September 2020; Accepted 25 October 2020
Available online 9 November 2020

dispersion and the degree of nonlinearity by making use of a few vertical layers, while they use first-order spatial derivatives. A detailed comparison between the aforementioned wave model approaches can be found in Kirby (2016) and Bai et al. (2018). SWASH (Zijlema et al., 2011) is a representative non-hydrostatic wave model and is based on the nonlinear shallow water equations with non-hydrostatic pressure.

The correct simulation of the waves in the nearshore zone requires the accurate modelling of all the processes involved, such as the generation of the waves, their propagation, transformation and reflection or absorption at the domain boundaries. There are three main methods to generate waves in numerical models. Method 1: weakly reflective wave generation (e.g. Higuera et al., 2013b; Wei and Kirby, 1995; Zijlema et al., 2011), method 2: moving boundary wave generation (e.g. Altomare et al., 2017; Grilli et al., 2002; Grilli and Horrillo, 1997; Higuera et al., 2015; Orszaghova et al., 2012), and method 3: internal wave generation (e.g. Altomare et al., 2018; Jacobsen et al., 2012; Larsen and Dancy, 1983; Lee et al., 2001; Schäffer and Sørensen, 2006; Wei et al., 1999).

Method 1 is the most popular since the computational cost is the least. According to this method, the horizontal velocity components of the target incident waves are imposed at the boundary of the computational domain over the vertical direction. In addition, in order to avoid reflections in front of the wave generator, a weakly reflective boundary condition is applied at the same location, according to which the total velocity is a linear superposition of the velocity of the target waves and the velocity of the waves propagating towards the boundary. This method is making use of the assumption that the waves propagating towards the boundary of the computational domain are shallow water waves with small amplitude and direction perpendicular to the domain boundary and thus, this method is considered weakly reflective when dispersive and directional waves are examined. Method 2 mimics the exact behavior of wave generation paddles of the experimental facilities by applying a moving boundary to generate and absorb waves, while the validity of the absorption is similar to method 1. Models that are using sponge layers, on the other hand, can absorb waves of different frequencies effectively with minimal reflection. To make this absorption optimal, each specific case requires tuning of the sponge layer thickness based on the lowest frequency component that has to be absorbed. The presence of the sponge layers requires that the generation of the waves takes place inside the computational domain and not on the boundary. In method 3, a spatially distributed mass or pressure forcing is added in the continuity or momentum equation, respectively, to internally generate waves, while numerical wave absorbing sponge layers are applied to absorb waves. The derivation of method 3 requires the knowledge of the underlying model equations, and thus its formulation differs depending on the governing equations. Although method 3 makes use of a larger numerical domain and thus the computational cost is higher, it is advantageous compared to the other two methods when it comes to the study of the interaction of the waves with structures (e.g., breakwaters, reefs, artificial islands) and wave energy converter (WEC) farms, where dispersive and directional waves are reflected or radiated back to the numerical domain boundary. Note, however, that the size of the sponge layers is usually significantly smaller than the area of interest in view of the coastal wave models (e.g. Boussinesq-type, non-hydrostatic models).

The present paper features a continuation of the study performed in Vasarmidis et al. (2019b), where the internal wave generation was mathematically derived and implemented initially in a non-hydrostatic wave model, SWASH. The method was validated with simple analytical solutions. In this study, however, several new aspects of the method have been investigated. To start with, the internal wave generation, method 3, for SWASH is further developed for short-crested waves. Further, in order to evaluate the method's performance with respect to its ability to accurately generate highly dispersive regular and irregular long-crested and short-crested waves and to avoid reflections at the location of the wave generator, the model was validated against analytical solutions and experimental data. Two benchmark experimental tests have been used, which include wave propagation over a shoal and wave diffraction around a vertical wall. Finally, a comparison is carried out between the performance of the newly developed internal wave generation (method 3) in non-hydrostatic models and the traditional weakly reflective wave generation (method 1) for the case of waves that are reflected back to the numerical boundary due to the presence of a structure.

The structure of the paper is presented as follows. The governing equations of the numerical model SWASH, the weakly reflective boundary and the implemented internal wave generation are described in Section 2. Section 3 provides a detailed presentation of the results of the SWASH model for the case of regular and irregular short-crested waves, where these results are compared with analytical solutions. In addition, validation results are presented in comparison with experimental data in Section 4, in order to evaluate the accuracy of the newly developed model. A comparison between the performance of methods 1 and 3 is presented in Section 3 and 4. The final section includes the conclusions of the present study.

2. SWASH model

2.1. Mathematical formulation

SWASH is an open source non-hydrostatic wave model (Zijlema et al., 2011) and has admittedly reached a mature stage in the field of wave transformation in coastal environments, as it allows for the incorporation of nonlinear shallow-water effects, like bound sub- and super-harmonics and near-resonant triad interactions (Rijnsdorp et al, 2014, 2015; Smit et al., 2014). Some recent applications of the model include wave overtopping (Suzuki et al., 2017), wave runup (Nicolae Lerma et al., 2017), wave forces (Gruwez et al., 2020) and the interaction of waves with vegetation (Suzuki et al., 2019) and wave energy converters (Rijnsdorp et al., 2018).

The model is developed following the Euler equations for an incompressible fluid with a free surface η and a constant density ρ_0 and for the case of a 3D domain the governing equations are given as follows:

$$\frac{\partial u}{\partial x}+\frac{\partial v}{\partial y}+\frac{\partial w}{\partial z}=0 \tag{1}$$

$$\frac{\partial u}{\partial t}+\frac{\partial uu}{\partial x}+\frac{\partial uv}{\partial y}+\frac{\partial uw}{\partial z}=-\frac{1}{\rho_0}\frac{\partial(p_h+p_{nh})}{\partial x} \tag{2}$$

$$\frac{\partial v}{\partial t}+\frac{\partial vu}{\partial x}+\frac{\partial vv}{\partial y}+\frac{\partial vw}{\partial z}=-\frac{1}{\rho_0}\frac{\partial(p_h+p_{nh})}{\partial y} \tag{3}$$

$$\frac{\partial w}{\partial t}+\frac{\partial wu}{\partial x}+\frac{\partial wv}{\partial y}+\frac{\partial ww}{\partial z}=-\frac{1}{\rho_0}\frac{\partial p_{nh}}{\partial z} \tag{4}$$

where x, y and z are the Cartesian coordinates, u and v are the horizontal velocity components in x-direction and y-direction, w is the vertical velocity component in z-direction, t is the time, p_h is the hydrostatic and p_{nh} is the non-hydrostatic pressures. The kinematic conditions at the free surface $z=\eta$ and the bottom $z=-d$, where d is the still water depth, are given in Eqs. (5) and (6), respectively:

$$w=\frac{\partial \eta}{\partial t}+u\frac{\partial \eta}{\partial x}+v\frac{\partial \eta}{\partial y} \tag{5}$$

$$w=-u\frac{\partial d}{\partial x}-v\frac{\partial d}{\partial y} \tag{6}$$

The free surface equation is obtained by integrating Eq. (1) for the entire water column $H=d+\eta$ and applying the kinematic condition at the free surface (Eq. (5)):

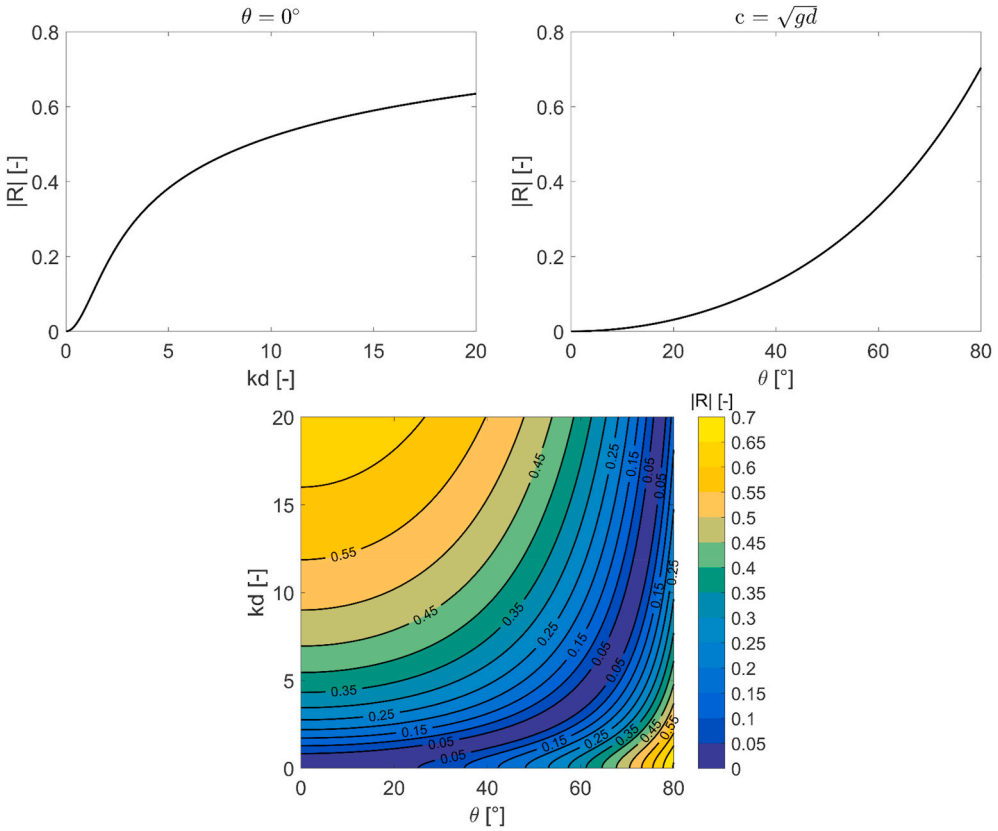

Fig. 1. Absolute reflection coefficient as a function of the incident wave angle θ and the dimensionless depth kd for the case that $c_0 = \sqrt{gd}$ and $\alpha = 0°$.

$$\frac{\partial \eta}{\partial t} + \frac{\partial}{\partial x}\int_{-d}^{\eta} u\,dz + \frac{\partial}{\partial y}\int_{-d}^{\eta} v\,dz = 0 \tag{7}$$

For the case that the number of layers in the vertical direction is K, Eq. (7) can be rewritten as:

$$\frac{\partial \eta}{\partial t} + \frac{\partial Q_{u,K}}{\partial x} + \frac{\partial Q_{v,K}}{\partial y} = 0, \qquad Q_{u,K} = \sum_{k=1}^{K} h_{u,k}u_k \text{ and } Q_{v,K} = \sum_{k=1}^{K} h_{v,k}v_k \tag{8}$$

where $h_{u,k}$, $h_{v,k}$ and u_k, v_k are the thicknesses and the layer-integrated horizontal velocities, respectively, corresponding to the k-th layer.

Sponge layers (relaxation zones) can be applied at the boundaries of the computational domain in order to prevent reflections back into the domain. In SWASH, the method proposed by Mayer et al. (1998) is implemented, according to which the velocity components and the free surface elevation are relaxed at each time step. Additionally, in case that a small number of layers in the vertical direction are applied, wave breaking is reproduced according to the method described in Smit et al. (2013). A thorough presentation of the governing equations and the numerical methods that are implemented in SWASH can be found in Zijlema et al. (2011) and Zijlema and Stelling (2008).

For all the test cases that are examined in the present study, in the horizontal direction a rectangular and uniform computational grid has been applied, in which the grid cell resolution is determined by the condition of having at least 50 grid cells per peak wave length. Additionally, an automatic time step control is applied during the simulation based on the CFL (Courant–Friedrichs–Lewy) condition, according to which the time step is halved when the Courant number is larger than a maximum value and is doubled when the Courant number is smaller than a minimum value. In the present study a maximum and a minimum Courant number of 0.5 and 0.2 is used respectively.

2.2. Weakly reflective boundary

According to the weakly reflective wave generation boundary that is implemented in SWASH, the inflow depth-averaged horizontal velocity at the boundary for the case of one layer is given by:

$$u(t) = \frac{\omega}{kd}\eta_t + \frac{c_0}{dcos\alpha}(\eta_t - \eta_i) \tag{9}$$

where k is the wave number, ω is the angular frequency, c_0 is the local linear wave speed, α is the wave propagation angle, η_t and η_i are the target and the instantaneous surface elevations, respectively. In case of a multi-layer formulation of the model, the inflow horizontal velocity is described by a hyperbolic cosine profile. The values of c_0 and α should be chosen a priori from the user and in case that the wave propagates towards the boundary of the computational domain with a wave speed of $c = \omega/k = c_0$ and with a wave angle of $\theta = \alpha$, then the wave will be perfectly absorbed at the boundary (Higdon, 1987).

Eq. (9) is obtained by combining the Sommerfeld condition with a 1D approximation of the continuity equation (Blayo and Debreu, 2005):

$$\frac{\partial \eta}{\partial t} + \frac{c_0}{cos\alpha}\frac{\partial \eta}{\partial x} = 0 \tag{10}$$

$$\frac{\partial \eta}{\partial t} + d\frac{\partial u}{\partial x} = 0 \tag{11}$$

Substituting Eq. (10) into Eq. (11) we get:

$$\frac{\partial u}{\partial x} - \frac{c_0}{d\ cos\alpha}\frac{\partial \eta}{\partial x} = 0 \tag{12}$$

The plane wave solution of Eqs. 10–12 can be written as:

$$\eta = \eta_1\ exp[i(\omega t - kxcos\theta)] + \eta_2 exp[i(\omega t + kxcos\theta)] \tag{13}$$

$$u = u_1\ exp[i(\omega t - kxcos\theta)] + u_2 exp[i(\omega t + kxcos\theta)] \tag{14}$$

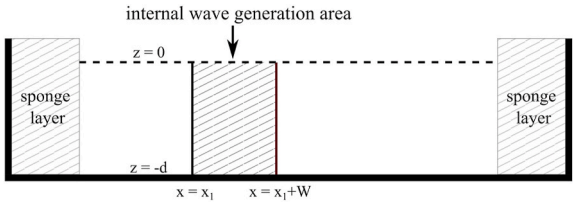

Fig. 2. Internal wave generation method definition in a 2D vertical domain.

where the subscripts 1 and 2 stand for incoming and reflected modes, respectively. Substituting Eqs. (13) and (14) in Eq. (11) gives:

$$u_1 - u_2 = \frac{\omega}{kdcos\theta}(\eta_1 + \eta_2) \tag{15}$$

Substituting Eqs. (13) and (14) in Eq. (12) we obtain:

$$u_1 - u_2 = \frac{c_0}{dcos\alpha}(\eta_1 - \eta_2) \tag{16}$$

Finally, eliminating u_1 and u_2 using Eq. (15), the reflection coefficient can be obtained:

$$R = \frac{\eta_2}{\eta_1} = -\frac{c\ \ cos\alpha - c_0 cos\theta}{c\ \ cos\alpha + c_0 cos\theta} \tag{17}$$

It can be noticed that the amount of reflection is indeed zero for the case that the incoming wave speed is equal to c_0 and the incident wave angle is equal to α. In Fig. 1, the absolute reflection coefficient as a function of the incident wave angle θ and the dimensionless depth kd is plotted for the case that $c_0 = \sqrt{gd}$ and $\alpha = 0^\circ$ which are the conditions that have been applied in the present study. It can be clearly observed that the absolute reflection coefficient increases for larger values of dimensionless depth kd and wave angle θ. The reason that the shallow water wave speed ($c_0 = \sqrt{gd}$) is used as an input, is based on the fact that in most nearshore applications the high frequency energy is dissipated near the shoreline while the long waves are reflected back. However, in case that man-made structures are considered, both short and long waves are reflected back towards the wave generation boundary with a range of wave speeds that cannot be estimated a priori. This problem can be partly alleviated through the extension of the Sommerfeld condition (Eq. (10)) by means of rational polynomials in kd of the dispersive wave celerity, $c_0 = c_0(kd)$, along with the second-order vertical derivative of the surface elevation (Wellens and Borsboom, 2020). Yet, this approach is less suitable for non-hydrostatic models using a few layers.

2.3. Internal wave generation

Vasarmidis et al. (2019b) developed an internal wave generation (method 3) for the SWASH model, similar to the source function proposed by Wei et al. (1999) for the depth averaged Boussinesq-type equations and this method has been made freely available through SWASH 6.01. According to this method, a spatially distributed mass is added in the free surface equation over an area called the "wave generation source area", while sponge layers (relaxation zones) are used at the domain boundaries to absorb the incoming waves (Fig. 2). In cases of dispersive and directional waves, method 3 can be effectively applied to avoid reflections at the boundary due to the use of method 1, as described in Section 2.2.

For a single wave component the source function is defined as follows (Wei et al., 1999):

$$f(x, y, t) = g(x)Dcos(\omega t - kysin\theta) \tag{18}$$

where g(x) is the shape of the source function, which is chosen to follow the Gaussian distribution and D is the amplitude of the source function, given by (Vasarmidis et al., 2019b):

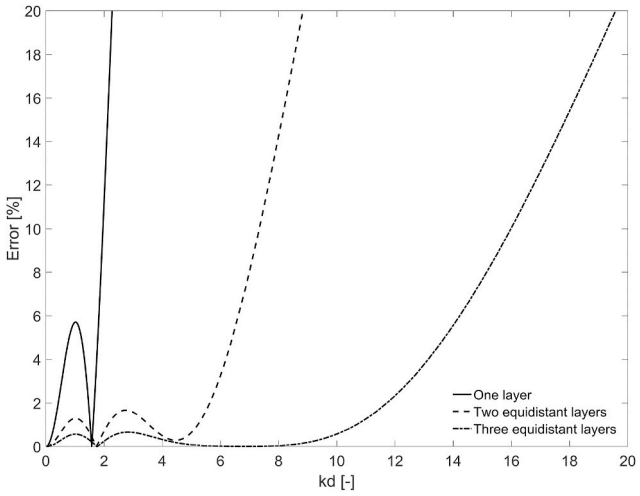

Fig. 3. Comparison of relative error in the normalised energy velocities C_e/C_{gAiry} for one, two and three vertical layers as function of the dimensionless depth kd.

$$D = 2C_e\eta_0\frac{cos\theta}{I} \tag{19}$$

where C_e is the energy velocity, and I is an integral defined by (Wei et al., 1999):

$$I = \sqrt{\frac{\pi}{\beta}}exp\left(-\frac{(kcos\theta)^2}{4\beta}\right) \tag{20}$$

where β has a value of $\beta = 20/W^2$ and W represents the width of the wave generation source area. The width of the source area is related to the target wave length L by using the auxiliary coefficient δ as $W = \delta L/2$. For all the simulations of the present study, δ is in the range of 0.5–0.8 (defined after iterations), where the larger values stand for larger wave heights.

The exact expression for the energy velocity C_e for the system of SWASH equations has been mathematically derived by Vasarmidis et al. (2019b) for the case of two equidistant vertical layers and is proved to be equal to the group velocity $C_g = d\omega/dk$ (Eq. (22)). In the present study, the energy velocity C_e for one and three equidistant vertical layers is also introduced (Eq. (21) and (23)).

$$C_{e,1} = \frac{8\sqrt{dg}}{\sqrt{\left(4 + (kd)^2\right)^3}} \tag{21}$$

$$C_{e,2} = \frac{64\sqrt{dg}\left(256 + 32(kd)^2 + 5(kd)^4\right)}{\sqrt{\left(16 + (kd)^2\right)\left(256 + 96(kd)^2 + (kd)^4\right)^3}} \tag{22}$$

$$C_{e,3} = \frac{72\sqrt{dg}\left(5038848 + 933120(kd)^2 + 147744(kd)^4 + 3024(kd)^6 + 35(kd)^8\right)}{\sqrt{\left(1296 + 120(kd)^2 + (kd)^4\right)\left(46656 + 19440(kd)^2 + 540(kd)^4 + (kd)^6\right)^3}} \tag{23}$$

The rational expression of the energy velocity C_e for the system of SWASH equations has been derived by using the linearized governing equations. This means that Eqs. 21–23 are less accurate in case that the target generated wave is highly non-linear.

In Fig. 3, the relative error in the normalised energy velocities C_e/C_{gAiry} is plotted for one, two and three vertical layers as a function of the dimensionless depth kd. It can be noticed that the relative error is getting smaller as the number of layers increases, which extends the applicability of the model to higher values of kd (dispersive waves) and thus the achieved accuracy to deeper water. For three vertical layers the

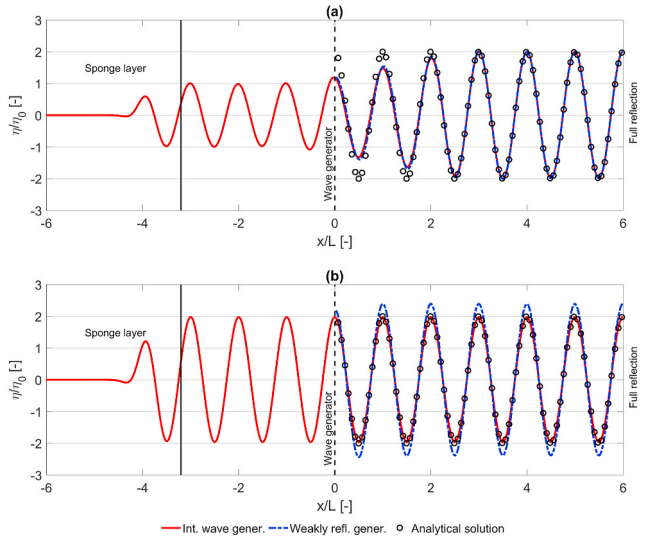

Fig. 4. Snapshots of normalised water surface elevations η/η_0 at (a) t = 28T and (b) t = 100T using internal wave generation (method 3, red solid line) and weakly reflective wave generation (method 1, blue dashed line) compared with the analytical solution (black circles) for the case of dispersive waves. (For interpretation of the references to colour in this figure legend, the reader is referred to the Web version of this article.)

corresponding relative error in the normalised energy velocity C_e/C_{gAiry} is smaller than 3% for kd $\leq$ 12.5. In this way, the developed method avoids the limitation that Choi and Yoon (2009) and Ha et al. (2013) have observed, where the applied internal wave generation in their models, was not accurate for deeper water conditions.

As a result, the free surface equation inside the wave generation source area for the case that the number of layers in the vertical direction is K, is given by:

$$\frac{\partial \eta}{\partial t}+\frac{\partial Q_{u,K}}{\partial x}+\frac{\partial Q_{v,K}}{\partial y}=2g(x)C_{e,K}\eta_0\cos(\omega t-kysin\theta)\frac{cos\theta}{I} \quad (24)$$

where $C_{e,K}$ is the energy velocity for K number of layers. Using Eq. (24) the temporal evolution of the free surface is calculated inside the source area and subsequently the new layer thicknesses are determined for each time step. In this way the source mass is distributed over the water column.

3. Validation with analytical solutions

3.1. Reflected dispersive waves

In order to check the performance of the proposed generation method (method 3) for handling reflected dispersive waves and to compare it with the performance of the weakly reflective wave generation method (method 1), a computational domain (12L long, where L is the wave length) with a sponge layer at the left boundary ($-6L \leq x \leq -3L$) and a closed right boundary (fully reflective wall, x = 6L) is used. The wave generation source area is placed at the middle of the computational domain (x = 0). The domain for method 1 is halved ($0 \leq x \leq 6L$) with the weakly reflective wave generator positioned at the left boundary (x = 0) and a fully reflective wall positioned at the right boundary (x = 6L). The generated waves have a height of H = 0.02 m and a period of T = 3.0 s, while the still water depth is d = 10 m and the dimensionless depth is kd = 4.5. The model is applied with two equidistant vertical layers (error < 3% for kd $\leq$ 6.0, Fig. 3), a uniform grid resolution of $\Delta x = 0.3$ m and an initial time step of $\Delta t = 0.0125$ s.

Fig. 4 shows two snapshots of normalised water surface elevations η/η_0 (where η_0 is the generated wave amplitude) at t = 28T and t = 100T,

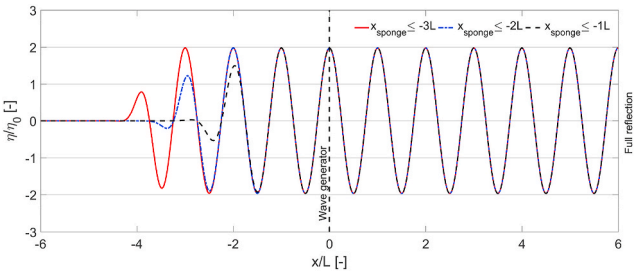

Fig. 5. Snapshots of normalised water surface elevations η/η_0 at t = 100T using internal wave generation for three different sponge layer positions, $x_{sponge} \leq$ -3L (red solid line), $x_{sponge} \leq$ -2L (blue dash-dot line) and $x_{sponge} \leq$ -1L (black dashed line). (For interpretation of the references to colour in this figure legend, the reader is referred to the Web version of this article.)

generated using internal (method 3, red solid line) and weakly reflective (method 1, blue dashed line) wave generation. The waves that are generated at the source area propagate towards both sides of the computational domain. The right boundary is fully reflecting the incoming waves, while the sponge layer on the other end is absorbing them. On the other hand, for method 1 the waves are generated at the left boundary and propagate towards the right boundary. At the right boundary, full reflection of the incoming waves occurs, while at the weakly reflective boundary the waves are being absorbed. Additionally, the target wave has the form of a linear wave and the horizontal dimension of the computational domain is an integer number of the considered wave length. The above gives as a result a theoretical profile (black circles) that has a known analytical expression from literature and is a standing wave with perfect nodal points.

In Fig. 4a, where the reflected waves have not yet arrived at the generation point, the water surface elevations, computed using wave generation methods 1 and 3, are identical and in excellent agreement with the analytical solution. However, in Fig. 4b the profile generated with method 1 differs significantly from the analytical solution. On the other hand, the profile generated with method 3 agrees very well with the analytical solution. The reflected dispersive waves pass through the internal wave generation area without affecting the generated waves and are fully absorbed by the sponge layer. Method 1 is not applicable in this case since the assumption that the waves propagating towards the boundary of the computational domain are shallow water waves with a phase velocity of $c = \sqrt{gd}$ is not valid and thus reflections are created. The theoretical reflection coefficient for the weakly reflective boundary as a function of the incident wave angle θ and the dimensionless depth kd is derived in Section 2.2. For kd = 4.5 the theoretical reflection coefficient is 37% (Fig. 1) and the calculated one is 39% (Fig. 4).

Additionally, it has to be mentioned that when using method 1, a sharp decrease of the wave height was noticed at the first computational cells next to the weakly reflective wave generation boundary. This is happening due to the fact that the hyperbolic profile of the target velocity component cannot be accurately described when coarse vertical resolution is used and thus method 1 needs calibration in case of deep water waves, to generate accurately the target wave height. For the case of irregular waves this calibration is becoming even more difficult, since the behavior of the generation boundary is different for each frequency component. On the other hand, method 3 that is presented in this study does not need any calibration, since the method is directly connected with the surface elevation (Eq. (24)) rather than the horizontal velocity component.

Finally, the influence of the distance between the sponge layer and the center of the wave generation source area has been examined. Two additional simulations have been executed with the sponge layer at the left boundary located at $-6L \leq x \leq -2L$ and $-6L \leq x \leq -1L$. The resulted normalised water surface elevations η/η_0 at t = 100T are shown in Fig. 5, where it can be noticed that the resulted profiles are identical

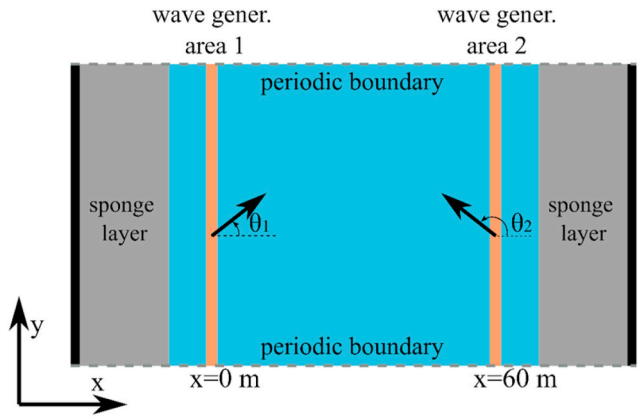

Fig. 6. Definition sketch for the case of two internal wave generators at x = 0 m and x = 60 m.

for all the cases outside the sponge layer zone. The above comparison leads to the conclusion that the sponge layer can be positioned at a distance of only one wave length from the wave generation area without influencing the results and thus the computational area and subsequently the computational cost can be reduced.

3.2. Oblique waves in a numerical basin with constant depth

In this section, the performance of the proposed internal wave generation method (method 3) for handling incoming oblique waves, that are propagating in a numerical basin with constant depth by using two internal wave generation areas (Fig. 6), is examined. The numerical basin is 210 m long in x-direction, 60 m wide in y-direction and 1 m deep. The internal wave generation areas are parallel to the y-axis and are positioned at a distance of 75 m from the left and right boundaries (x = 0 m and x = 60 m). Sponge layers are placed behind the wave generation areas with a width of 60 m, while periodic conditions are applied at the top and bottom boundaries of the computational domain.

The generated waves have a height of H = 0.01 m, a period of T = 4.0 s and a dimensionless depth of kd = 0.52. One vertical layer is applied since the error is smaller than 3% for kd ≤ 0.55 in case of one layer (Fig. 3). Two different wave propagation angle combinations are examined, one with $\theta_1 = 15^\circ$, $\theta_2 = 195^\circ$ and one with $\theta_1 = 15^\circ$, $\theta_2 = 165^\circ$ where the subscripts 1 and 2 stand for the left (x = 0 m) and the right (x = 60 m) internal wave generators, respectively. θ is the angle between the positive x-axis and the propagation direction, measured counterclockwise. A uniform grid resolution of $\Delta x = \Delta y = 0.15$ m is used, while a duration of 120 s with a time step Δt = 0.0125 s is considered, targeting a steady state wave field.

The computed wave field (normalised water surface elevation η/η_0) is compared with the corresponding analytical solution at t = 30T, in Fig. 7 and Fig. 8. The computed solution agrees very well with the analytical one in the whole domain for both wave propagation angle combinations. The excellent agreement indicates that the internal wave generation is able to generate oblique waves and that oblique waves can pass through the wave generation area without any distortion.

It has to be mentioned that an internal wave generation area parallel to y-axis is not able to generate a wave which propagates along y-axis. For that reason, in case that the target incident wave forms an angle between −10° and 10° with the y-axis, an internal wave generation area parallel to x-axis should be applied. In addition, an L-shape wave generation layout can be used to generate oblique waves. According to this layout, two internal wave generations areas with sponge layers behind them are applied, one parallel to the y-axis and one parallel to the x-axis of the numerical domain. However, it has been shown (Vasarmidis et al., 2019a) that this layout leads to wave diffraction patterns inside the numerical domain, caused by the two wave generation areas intersecting with each other and interacting with the lateral sponge layers, and

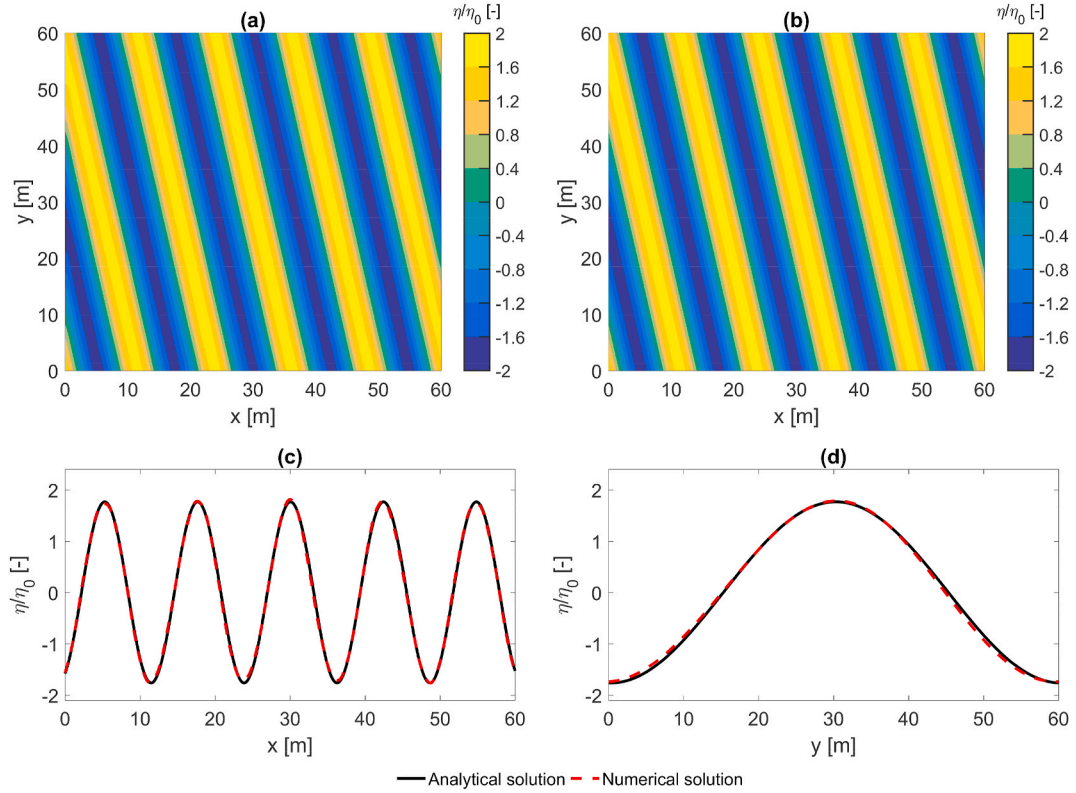

Fig. 7. Comparison between (a) computed and (b) analytical normalised water surface elevation η/η_0 at t = 30T for $\theta_1 = 15^\circ$, $\theta_2 = 195^\circ$:(c) cross section at y = 35 m (d) cross section at x = 18 m.

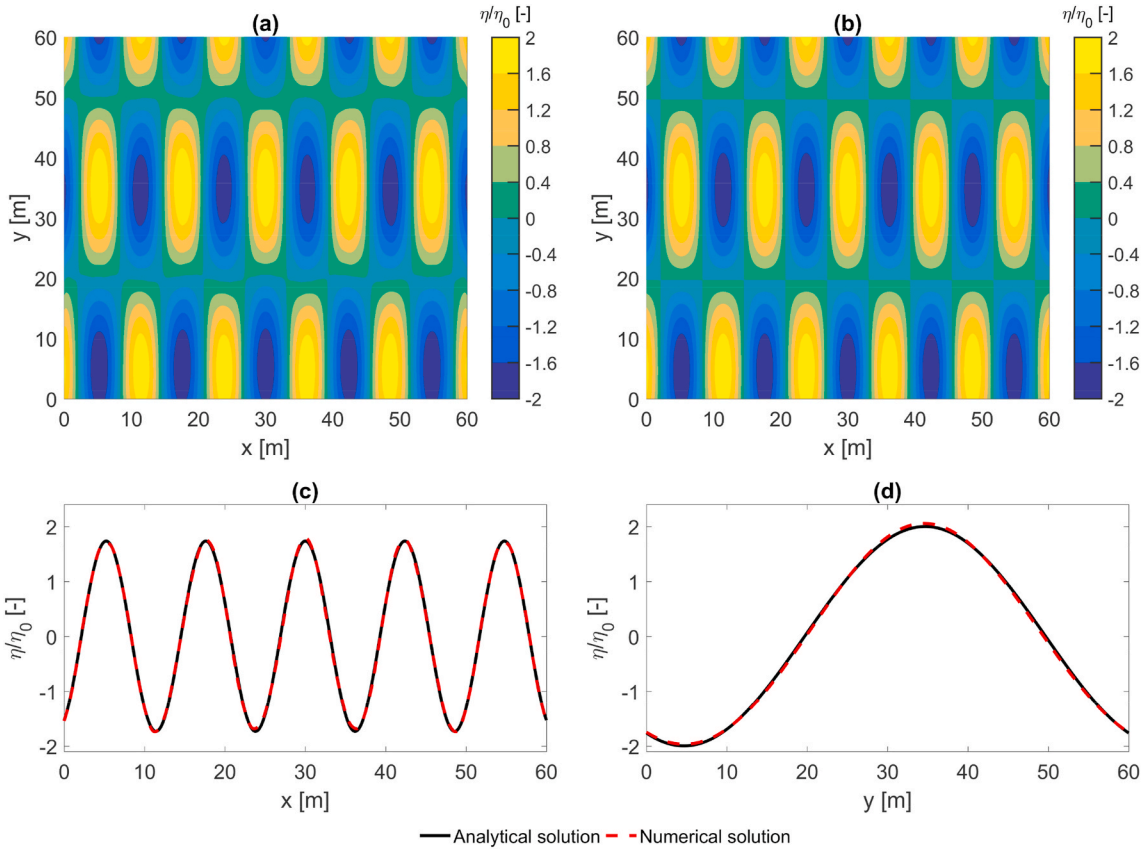

Fig. 8. Comparison between (a) computed and (b) analytical normalised water surface elevation η/η_0 at t = 30T for $\theta_1 = 15°$, $\theta_2 = 165°$:(c) cross section at y = 35 m (d) cross section at x = 18 m.

thus periodic lateral boundaries are preferred in order to avoid such diffractions.

3.3. Irregular short-crested waves in a numerical basin with constant depth

In this section, a test case of short-crested waves is considered, in which the target wave frequency spectrum is a JONSWAP spectrum, with a significant wave height $H_s = 0.5$ m, a peak wave period $T_p = 12.0$ s and a dimensionless depth kd = 0.48 for the peak frequency. The frequency range is defined between $0.5f_p$ and $3f_p$ and the peak enhancement factor is $\gamma = 3.3$. Two cases with spreading standard deviation $\sigma_\theta = 10°$ (swell waves) and $\sigma_\theta = 30°$ (wind waves) are examined. The numerical basin is 1500 m long, 500 m wide and 7.6 m deep. Sponge layers are placed at the right and left boundaries with a width determined by the peak wave length, while periodic conditions are applied at the top and bottom boundaries of the computational domain. The highest frequency ($3f_p$) and the lowest frequency ($0.5f_p$) are used to define the grid cell size and the initial time step Δt, respectively. Additionally, the following directional spreading function is employed (Frigaard et al., 1997):

$$D(f,\theta) = \frac{1}{\sqrt{\pi}}\frac{\Gamma(s_1+1)}{\Gamma\left(s_1+\frac{1}{2}\right)}\cos^{2s_1}(\theta-\theta_0), \quad -\frac{\pi}{2} < \theta-\theta_0 < \frac{\pi}{2} \tag{25}$$

where Γ is the Gamma function, s_1 is the directional spreading parameter, and θ_0 is the wave propagation angle. The relation between the spreading standard deviation, σ_θ, and the directional spreading parameter, s_1, is given by (Vasarmidis et al., 2019a):

$$\sigma_\theta = \sqrt{2 - \frac{2\Gamma^2(s_1+1)}{\Gamma\left(s_1+\frac{1}{2}\right)\Gamma\left(s_1+\frac{3}{2}\right)}} \tag{26}$$

The duration of the simulations is 3 h with a time step Δt = 0.05 s, while the wave synthesis method proposed by Sand and Mynett (1987) has been employed.

A group of 5 wave gauges measuring the surface elevations has been positioned in the center of the computational domain, following the configuration "CERC 5" proposed by Borgman and Panicker (1970). The measured time series of surface elevations are used to calculate the frequency spectra and the normalised spreading function distributions, which are compared with the analytical solution in Fig. 9 for spreading standard deviation $\sigma_\theta = 10°$ and $\sigma_\theta = 30°$. The agreement with the analytical solution for both cases is very good indicating that the proposed method 3 is capable of generating accurately the target short-crested wave field. A mismatch between the calculated and the analytical frequency spectra for $\sigma_\theta = 10°$ (Fig. 9a) can be observed in the frequency range of 0.15 Hz–0.18 Hz, where the model slightly overestimates the spectral density. This mismatch could be due to the position of the wave gauges with respect to the wave generation area or due to a small reflection from the sponge layers. However, this overestimation is not observed in the case of $\sigma_\theta = 30°$ (Fig. 9b).

4. Validation with experimental data

4.1. Wave propagation over a shoal

A three-dimensional version of the developed model with the internal wave generation, method 3, is applied to study regular and irregular waves propagating over an elliptic shoal. The experiment that was

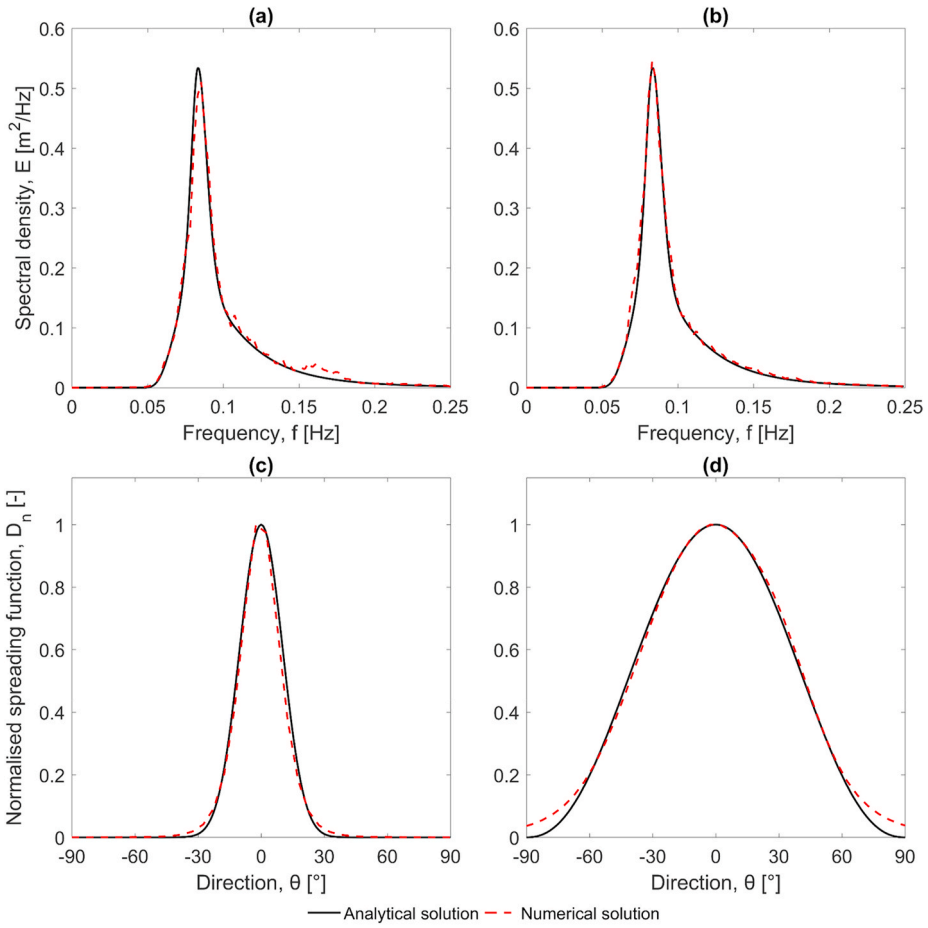

Fig. 9. The frequency spectra (top panels) and the normalised spreading function distributions (bottom panels) resulting from the use of method 3 (red dashed line), compared with the analytical solution (black solid line) for irregular short-crested waves with spreading standard deviation σ_θ of (a,c) 10° and (b,d) 30°. (For interpretation of the references to colour in this figure legend, the reader is referred to the Web version of this article.)

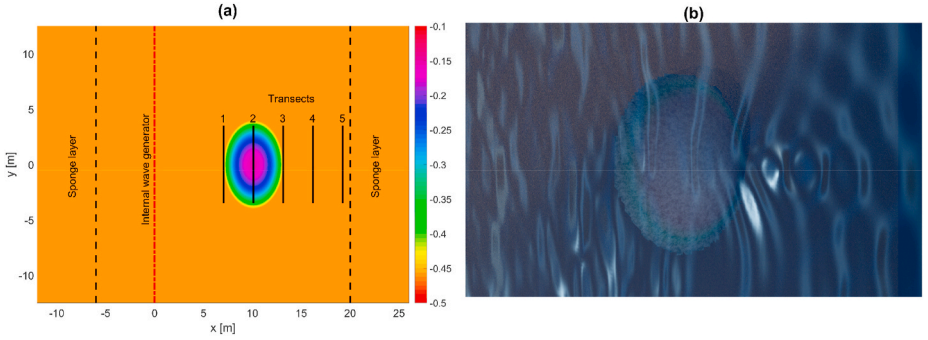

Fig. 10. (a) Bottom levels of the experimental setup as introduced in the numerical domain in SWASH, (b) 3D visualization of short-crested waves propagating over the shoal.

carried out by Vincent and Briggs (1989) has been repeatedly used as a standard test case for validating wave propagation models (Vasarmidis et al., 2019a) and hence it is used here for validation purposes of the present numerical model. It has to be mentioned that only the internal wave generation method is examined for this experimental layout, since there are no waves that are reflected back to the numerical wave generation boundary, and thus a similar behavior is to be expected when using the weakly reflective wave generation method (method 1).

The bathymetry of the experimental setup of Vincent and Briggs (1989) as implemented in SWASH is illustrated in Fig. 10 and is defined as:

$$\left(\frac{x}{3.05}\right)^2 + \left(\frac{y}{3.96}\right)^2 = 1 \tag{27}$$

$$d_e = -0.4572 + 0.7620\left\{1 - \left(\frac{x}{3.81}\right)^2 + \left(\frac{y}{4.95}\right)^2\right\}^{0.5} \tag{28}$$

where x and y are the coordinates with $x = y = 0$ at the center of the shoal and d_e is the bed level inside the shoal area. The shoal geometry follows the one used in the experiments of Berkhoff et al. (1982), but with a flat bottom ($d = 45.72$ cm) outside the shoal area.

In total 9 numerical test cases are executed including breaking and

Table 1
Numerical input wave conditions based on the Vincent and Briggs (1989) experimental wave conditions.

Test Case ID	(Peak) period, T, T_p (s)	(Significant) Wave Height H, H_s (cm)	Phillips constant, α [-]	Peak enhancement factor, γ [-]	Spreading standard deviation, σ_θ (°)
M1	1.3	5.50	–	–	–
U3	1.3	2.54	0.00155	2	0
N3	1.3	2.54	0.00155	2	10
B3	1.3	2.54	0.00155	2	30
U4	1.3	2.54	0.00047	20	0
N4	1.3	2.54	0.00047	20	10
B4	1.3	2.54	0.00047	20	30
N5	1.3	19.0	0.08650	20	10
B5	1.3	19.0	0.02620	2	30

non-breaking waves of the following types: regular waves, irregular long- and short-crested waves. The numerical and experimental input parameters for all the test series are listed in Table 1. The dimensionless depth is kd = 1.27 for the peak frequency and thus two equidistant vertical layers are applied. A uniform grid resolution of $\Delta x = \Delta y = 0.05$ m is used, while an automatic time step control is applied based on the CFL condition.

The target frequency spectrum is a TMA spectrum (Bouws et al., 1985) in all the irregular test cases where broad ($\gamma = 2$) and narrow ($\gamma = 20$) frequency spectra are examined. Additionally, the above spectra are combined with standard deviation $\sigma_\theta = 10°$ (narrow directional spreading) and $\sigma_\theta = 30°$ (broad directional spreading). The wave heights of the numerical model are obtained by sampling the surface elevation for 36.4 s and 260 s for the regular and irregular cases, respectively, similar to the experiment.

In Fig. 11 the resulted normalised wave heights H/H_0 of the numerical model (red lines) are compared with the experimental data (black circles) along five measurement transects (shown in Fig. 10a) for the case of regular waves (test case M1). As it can be observed, the numerical and the experimental data show a very good agreement.

The normalised wave heights along transect 4 for the cases of irregular non-breaking and breaking waves are presented in Fig. 12 and

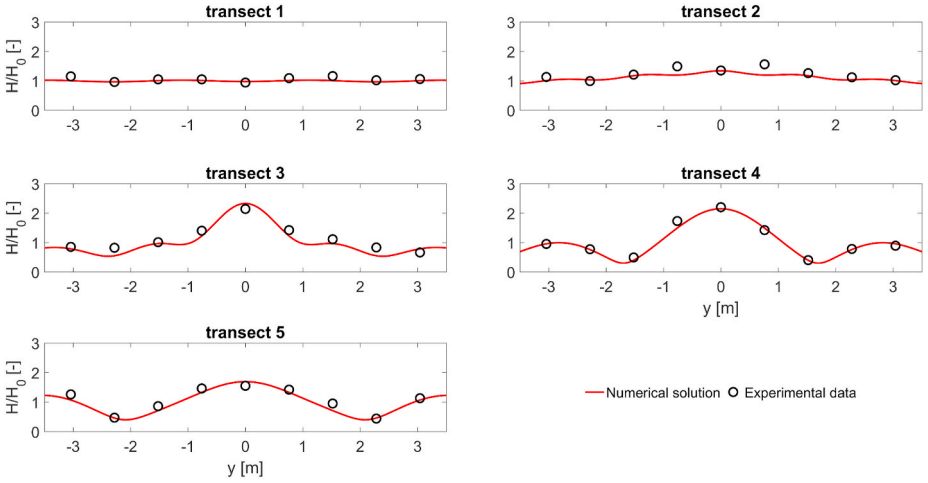

Fig. 11. Comparison of normalised wave heights H/H_0 between numerical model results (red solid lines) and experimental data (black circles) along different measurement transects for test case M1. (For interpretation of the references to colour in this figure legend, the reader is referred to the Web version of this article.)

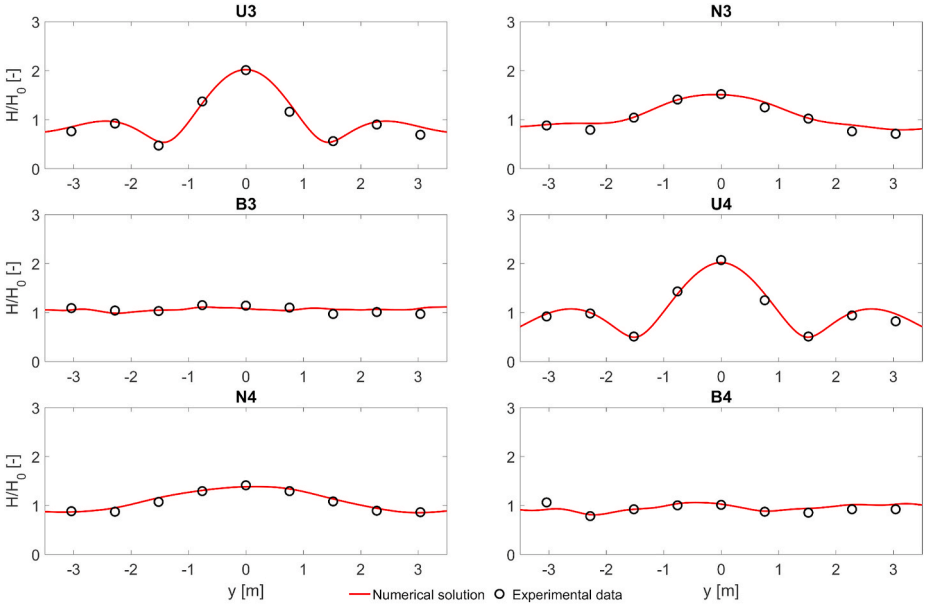

Fig. 12. Comparison of normalised wave heights H/H_0 between numerical model results (red solid lines) and experimental data (black circles) along transect 4 for non-breaking irregular waves. (For interpretation of the references to colour in this figure legend, the reader is referred to the Web version of this article.)

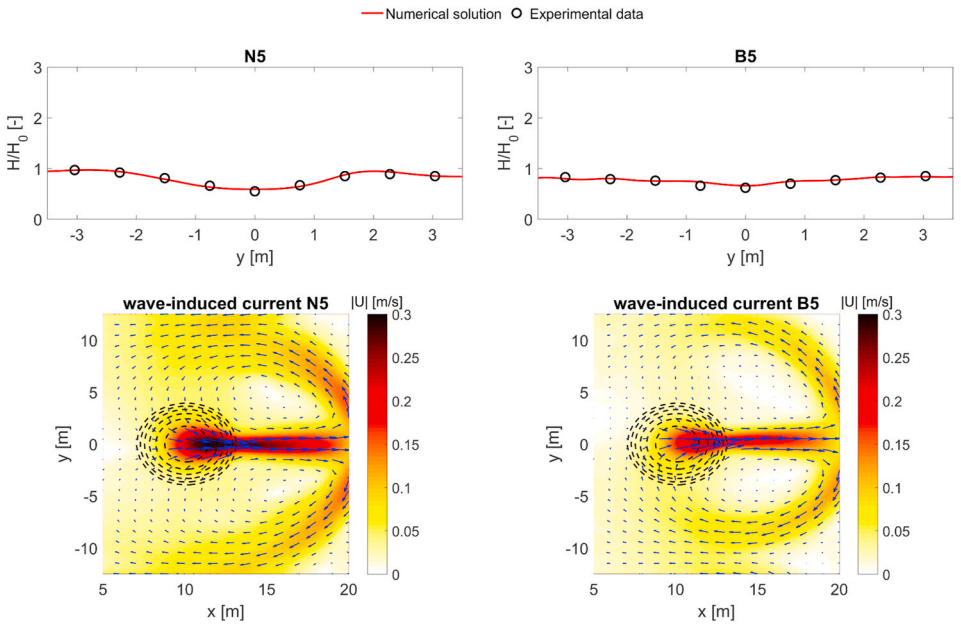

Fig. 13. Normalised wave heights H/H_0 along transect 4 and wave-induced currents for breaking irregular waves.

Table 2
Root mean square error (RMSE) and Skill factor for each test case.

Test case ID	U3	N3	B3	U4	N4	B4	N5	B5
RMSE	0.073	0.070	0.060	0.060	0.044	0.069	0.024	0.033
Skill	0.933	0.935	0.943	0.948	0.960	0.925	0.970	0.956

Fig. 13, respectively. SWASH correctly predicts the wave focusing due to the presence of the shoal for the case of non-breaking waves. The broad and narrow frequency spectra, test case U3 and U4 respectively, give a maximum normalised wave height at y = 0 with a value around 2.0. On the other hand, in test cases with directional spreading (test cases N3, B3, N4 and B4) it can be noticed that the influence of the shoal on the resulted wave field is reduced. For the case of breaking waves a reduction of the normalised wave height behind the shoal can be observed. This is happening due to the wave induced current (Fig. 13) which defocuses wave rays behind the shoal. Choi et al. (2009) proved that numerical models that neglect the effect of wave induced current are not able to predict the aforementioned physical process. In addition, the root mean square error (RMSE) and the Skill factor are utilized for each test case in order to evaluate the model capability to predict the normalised wave heights:

$$\mathrm{RMSE} = \sqrt{\frac{\sum_{i=1}^{N}(P_i - O_i)^2}{N}} \quad \mathrm{Skill} = 1 - \sqrt{\frac{\sum_{i=1}^{N}(P_i - O_i)^2}{\sum_{i=1}^{N} O_i^2}} \tag{29}$$

where O and P stand for the observed (experimental data) and predicted (model results) values, respectively. The small error and the high skill factor (Table 2) indicate that the model is able to correctly predict the transformation of waves propagating over a shoal.

4.2. Wave diffraction around a vertical wall

Finally, to verify the added value of the internal wave generation (method 3) in comparison with the weakly reflective wave generation boundary (method 1), simulations are conducted for regular and irregular waves diffracting around a breakwater. In this way, the two different wave generation methods will be evaluated for the case that

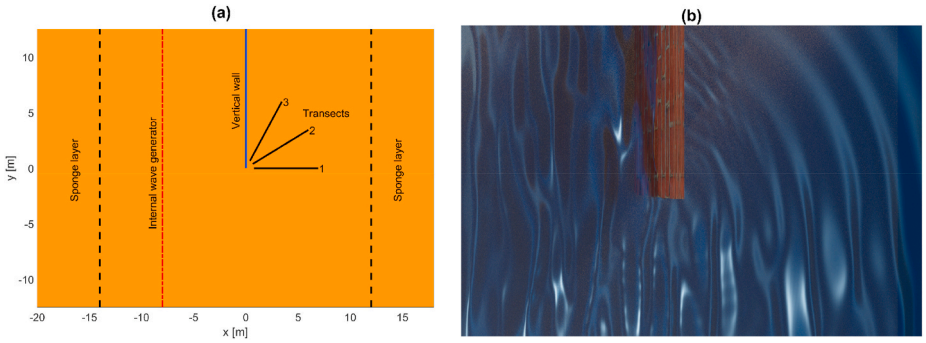

Fig. 14. (a) Experimental setup of Briggs et al. (1995) as introduced in the numerical domain in SWASH, (b) 3D visualization of short-crested waves diffracting around the vertical wall.

Table 3
Numerical input wave conditions based on the Briggs et al. (1995) experimental wave conditions.

Test Case ID	(Peak) period, T, T_p (s)	(Significant) Wave Height H, H_s (cm)	Phillips constant, α [-]	Peak enhancement factor, γ [-]	Spreading standard deviation, σ_θ (°)
M1	1.3	5.50	–	–	–
M4	1.3	7.75	–	–	–
N1	1.3	7.75	0.0144	2	10
N2	1.3	7.75	0.0044	20	10
B1	1.3	7.75	0.0144	2	30
B2	1.3	7.75	0.0044	20	30

oblique waves propagate back towards the generation area. The experiment of Briggs et al. (1995), where waves diffract around an impermeable vertical wall, is used here to validate the developed model.

The experimental setup consists of a vertical, rigid and thin wall which is positioned parallel to the wave paddles, extending from the centerline to the side wall of the basin. The bottom of the basin is flat with a still water depth of d = 45.72 cm, while wave absorber material is piled on the seaward side of the wall to minimize reflections. Detailed information on the experimental setup and results can be found in Briggs et al. (1995), where additionally, it is shown that the experimental results compared well with the theoretical methods for estimating diffraction.

The numerical basin is 46 m long ($-24 \leq x \leq 22$) and 25 m wide ($-12.5 \leq y \leq 12.5$). The internal wave generation area is parallel to the y-axis and is placed at a distance of 8 m ($x = -8$ m) from the vertical wall ($x = 0$ m). Closed lateral boundaries are used at $y = -12.5$ m and $y =$

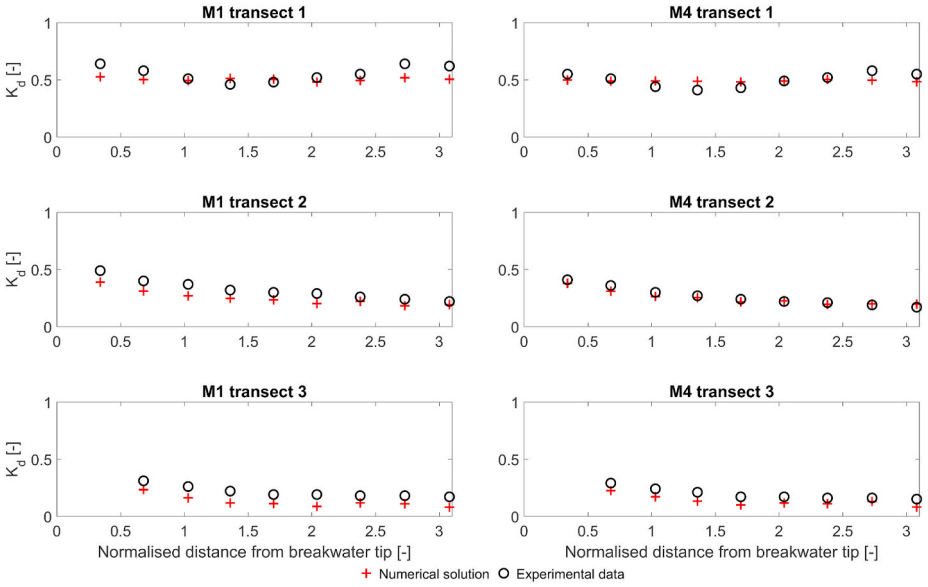

Fig. 15. Comparison of diffraction coefficients between numerical model results (red plus signs) and experimental data (black circles) for regular waves. (For interpretation of the references to colour in this figure legend, the reader is referred to the Web version of this article.)

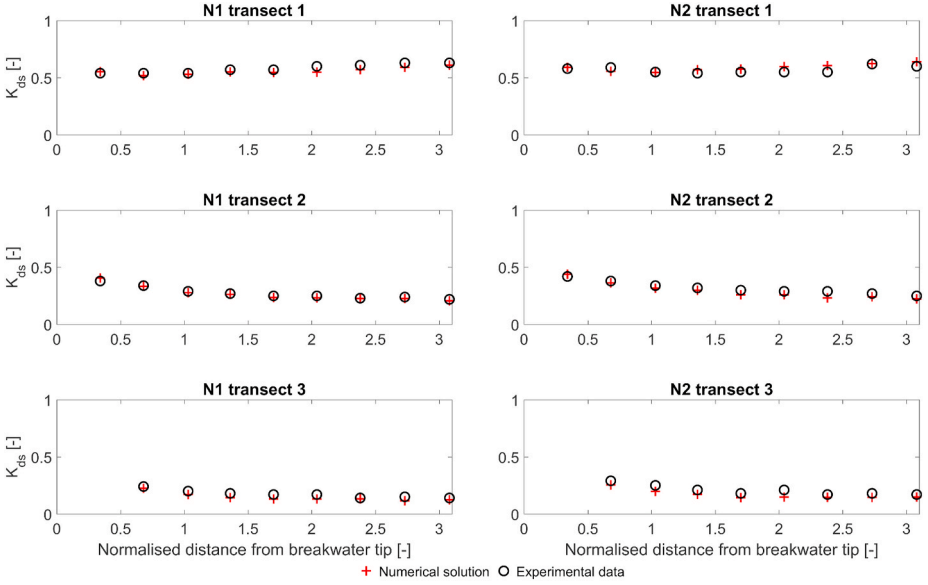

Fig. 16. Comparison of diffraction coefficients between numerical model results (red plus signs) and experimental data (black circles) for irregular waves with narrow directional spreading distribution. (For interpretation of the references to colour in this figure legend, the reader is referred to the Web version of this article.)

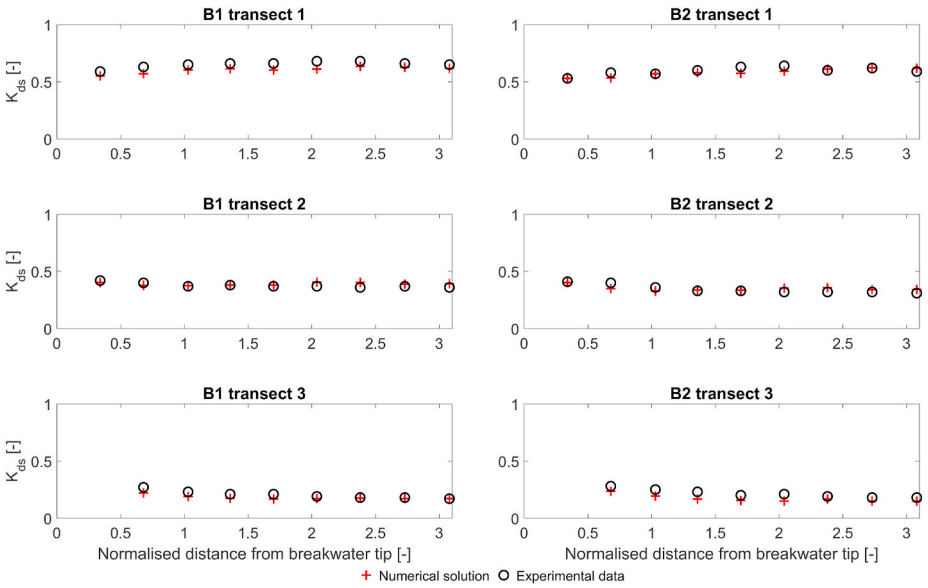

Fig. 17. Comparison of diffraction coefficients between numerical model results (red plus signs) and experimental data (black circles) for irregular waves with broad directional spreading distribution. (For interpretation of the references to colour in this figure legend, the reader is referred to the Web version of this article.)

12.5 m and sponge layers with a width of 10 m are placed at x = −14 m and x = 12 m (Fig. 14).

In total 6 numerical test cases are conducted: two with regular waves and four with irregular short-crested waves. The target wave characteristics are similar to those in Section 4.1 and are listed in Table 3. The dimensionless depth is kd = 1.27 for the peak frequency and thus two equidistant vertical layers are applied. The wave heights of the numerical model are obtained by sampling the surface elevation for 36.4 s and 260 s for the regular and irregular cases, respectively, along three measurement transects (Fig. 14a) that are forming an angle of 90° (transect 1), 60° (transect 2) and 30° (transect 3) with the wall tip. A uniform grid resolution of $\Delta x = \Delta y = 0.05$ m is used, while an automatic time step control is applied based on the CFL condition.

In Fig. 15, Fig. 16 and Fig. 17, comparisons of diffraction coefficients between numerical model results (red plus signs) and experimental data (black circles) for all test cases are presented. The diffraction coefficient K_d (K_{ds} for irregular) is computed as the ratio of the diffracted wave height H_d (H_{ds} for irregular) to the incident wave height H_i (H_s for irregular). The x-axis corresponds to the distance from the wall tip, normalised by the wave length ($L = L_p = 2.25$ m). In general, the agreement is very good between the numerical model and experimental results. The largest deviation is observed for the case of the regular waves (M1, M4), where the numerical model underpredicts the diffraction coefficients along measurement transect 3. On the other hand, the numerical model matches the observed values for the case of irregular short-crested waves very well along all the measurement transects. In addition, it can be observed that the wave penetration is greater for the case of the broad directional spreading distribution ($\sigma_\theta = 30°$), while the directional spreading affects the diffraction coefficients more rather than the frequency spreading.

Furthermore, the weakly reflective wave generation (method 1) has been used to simulate the above wave conditions. The numerical set up is the same as in the case with method 3, apart from the fact that the length of the domain is smaller ($-8 \leq x \leq 22$) since no sponge layer is used behind the generation line. Fig. 18 presents a comparison between the performance of the internal wave generation (method 3, red plus signs) and the weakly reflective generation (method1, blue circles) for predicting the diffraction coefficients observed by Briggs et al. (1995) experiment. To calculate the diffraction coefficient the generated wave height at the location of the tip of the wall in case of an empty basin (without the wall) has been used as incident wave height. In this way, the deficiency of the weakly reflective generation boundary to generate precisely the target wave height, as mentioned in Section 3.1, is not taken into account for the calculation of the RMSE. As it can be observed, the performance of the two wave generation methods is almost identical for the case of regular waves (M1, M4) despite the waves being slightly dispersive. This is happening due to the fact that the simulation time is only 54.6 s (sampling duration 36.4 s) similar to the experiment and thus the reflected waves due to the weakly reflective generation boundary have not yet reached the lee side of the wall. For longer simulations the wave fields inside the two numerical domains differ significantly, but they cannot be compared with the experimental data due to the reflections from the side walls. However, for the case of irregular waves where the simulation times are longer, the performance of method 3 is better, since the calculated RMSE for method 1 is at least double than the one corresponding to method 3. In addition, the RMSE of method 1 is larger in case of the broad directional spreading distribution especially along the transect 1. This can be explained by the fact that the waves are propagating back towards the generation boundary with a larger wave angle than in case of the narrow directional spreading distribution. In Section 2.2, where the theoretical reflection coefficient is derived for the weakly reflective boundary as a function of the incident wave angle θ, it can be observed that the reflection increases for larger incident wave angles (Fig. 1).

5. Conclusions

In the present study the application of internal wave generation method in the open source non-hydrostatic wave model, SWASH, is evaluated. According to this method, a spatially distributed mass is added in the free surface equation over an area to generate waves, while sponge layers are used at the domain boundaries to absorb the incoming waves. In the framework of the present study, the method is extended and validated for short-crested waves, enabling the study of long-existing engineering problems in a more accurate way. Test cases with man-made structures (e.g., breakwaters, artificial reefs, artificial islands) and wave energy converter (WEC) farms, where the reflected and radiated waves cannot be estimated a priori, can be examined. The applicability of the developed method to generate regular and irregular long-crested and short-crested waves is demonstrated using analytical solutions and two benchmark experiments, where the numerical model results show a very good agreement with the analytical solutions and

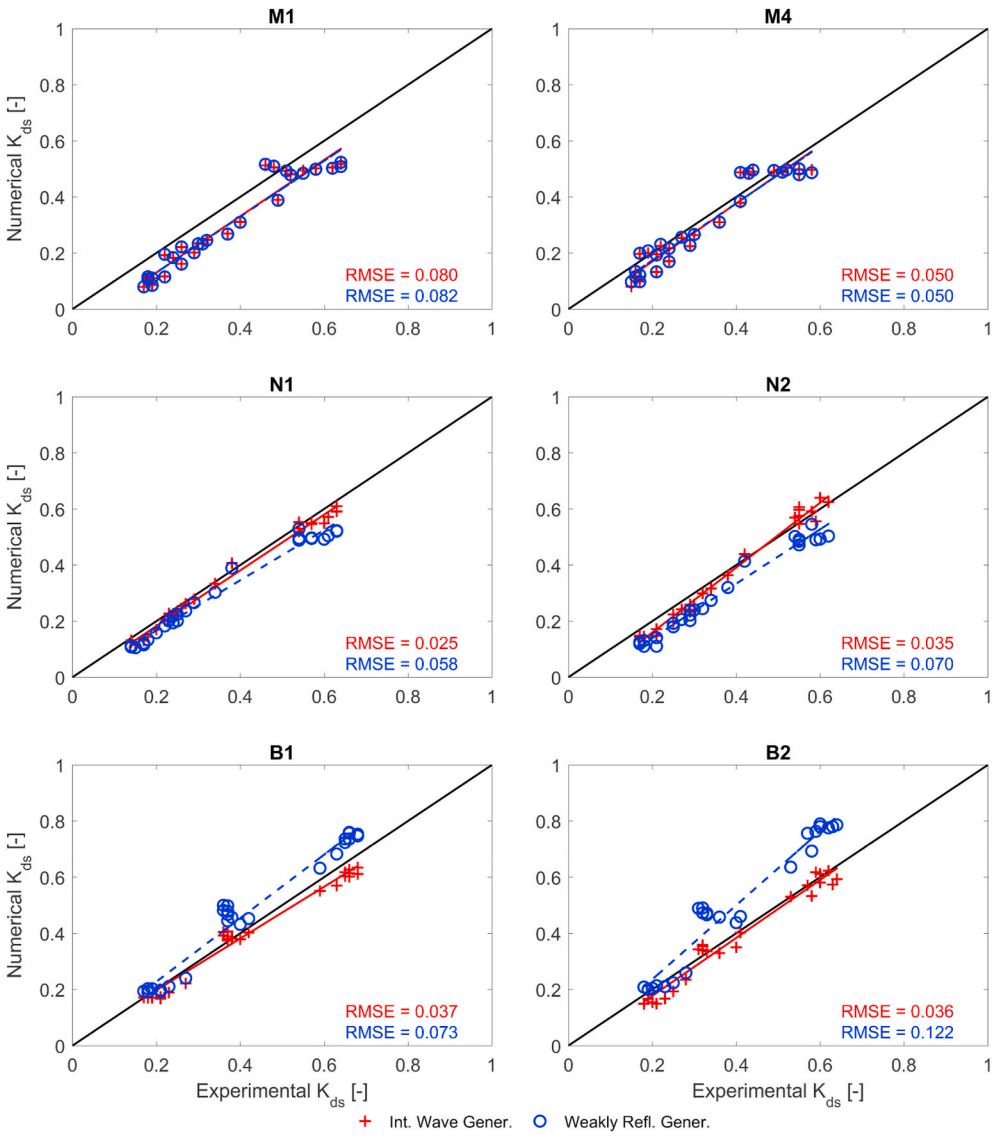

Fig. 18. Comparison between the performance of the internal wave generation (method 3, red plus signs) and the weakly reflective generation (method 1, blue circles) for predicting the diffraction coefficients observed by Briggs et al. (1995) experiment. Black solid lines represent perfect agreement, while red solid line and the blue dashed line are the fitting lines for method 3 and method 1, respectively. (For interpretation of the references to colour in this figure legend, the reader is referred to the Web version of this article.)

experimental data.

In addition, the performance of the internal wave generation (method 3) is compared with this of the weakly reflective wave generation boundary (method 1) for the case of waves that are reflected back to the numerical boundary due to the presence of a structure. The use of sponge layers in method 3 requires an extension of the numerical domain and thus the computational cost is higher compared to method 1. However, in the present study, it has been proven that the internal wave generation is advantageous compared to the weakly reflective generation boundary since it is able to generate more accurately the target wave characteristics even in case of highly dispersive and directional waves and at the same time any reflection due to the presence of the weakly reflective wave generator is avoided.

CRediT authorship contribution statement

Panagiotis Vasarmidis: Conceptualization, Software, Validation, Writing - original draft. **Vasiliki Stratigaki:** Resources, Supervision, Writing - review & editing. **Tomohiro Suzuki:** Software, Supervision, Writing - review & editing. **Marcel Zijlema:** Software, Supervision, Writing - review & editing. **Peter Troch:** Resources, Supervision, Writing - review & editing.

Declaration of competing interest

The authors declare that they have no known competing financial interests or personal relationships that could have appeared to influence the work reported in this paper.

Acknowledgement

This research was funded by Research Foundation—Flanders (FWO), Belgium. The first author, Panagiotis Vasarmidis, is Ph.D. fellow (fellowship 11D9618N) of the FWO (Fonds Wetenschappelijk Onderzoek - Research Foundation Flanders), Belgium. Vasiliki Stratigaki is a postdoctoral researcher (fellowship 1267321N) of the FWO (Fonds Wetenschappelijk Onderzoek - Research Foundation Flanders), Belgium.

References

Altomare, C., Domínguez, J.M., Crespo, A.J.C., González-Cao, J., Suzuki, T., Gómez-Gesteira, M., Troch, P., 2017. Long-crested wave generation and absorption for SPH-based DualSPHysics model. Coast. Eng. 127, 37–54. https://doi.org/10.1016/j.coastaleng.2017.06.004.

Altomare, C., Tagliafierro, B., Dominguez, J.M., Suzuki, T., Viccione, G., 2018. Improved relaxation zone method in SPH-based model for coastal engineering applications. Appl. Ocean Res. 81, 15–33. https://doi.org/10.1016/j.apor.2018.09.013.

Bai, Y., Cheung, K.F., 2012. Depth-integrated free-surface flow with a two-layer non-hydrostatic formulation. Int. J. Numer. Methods Fluid. 69, 411–429. https://doi.org/10.1002/fld.2566.

Bai, Y., Yamazaki, Y., Cheung, K.F., 2018. Convergence of multilayer nonhydrostatic models in relation to Boussinesq-type equations. J. Waterw. Port, Coast. Ocean Eng. 144, 1–10. https://doi.org/10.1061/(ASCE)WW.1943-5460.0000438.

Berkhoff, J.C.W., Booy, N., Radder, A.C., 1982. Verification of numerical wave propagation models for simple harmonic linear water waves. Coast. Eng. 6, 255–279. https://doi.org/10.1016/0378-3839(82)90022-9.

Blayo, E., Debreu, L., 2005. Revisiting open boundary conditions from the point of view of characteristic variables. Ocean Model. 9, 231–252. https://doi.org/10.1016/j.ocemod.2004.07.001.

Borgman, L.E., Panicker, N.N., 1970. Design Study for a Suggested Wave Gauge Array off Point Mugu. Hydraulic Engineering Laboratory, University of California at Berkeley, California. Technical Report 1–14.

Bouws, E., Günther, H., Rosenthal, W., Vincent, C.L., 1985. Similarity of the wind wave spectrum in finite depth water: 1. Spectral form. J. Geophys. Res. 90, 975. https://doi.org/10.1029/JC090iC01p00975.

Briggs, M.J., Thompson, E.F., Vincent, C.L., 1995. Wave diffraction around breakwater. J. Waterw. Port, Coast. Ocean Eng. 121, 23–35. https://doi.org/10.1061/(ASCE)0733-950X(1995)121:1(23).

Choi, J., Lim, C.H., Lee, J.I., Yoon, S.B., 2009. Evolution of waves and currents over a submerged laboratory shoal. Coast. Eng. 56, 297–312. https://doi.org/10.1016/j.coastaleng.2008.09.002.

Choi, J., Yoon, S.B., 2009. Numerical simulations using momentum source wave-maker applied to RANS equation model. Coast. Eng. 56, 1043–1060. https://doi.org/10.1016/j.coastaleng.2009.06.009.

Frigaard, P., Helm-Petersen, J., Klopman, G., Stansberg, C.T., Benoit, M., Briggs, M.J., Miles, M., Santas, J., Schäffer, H.A., Hawkes, P.J., 1997. IAHR List of Sea Parameteres: an update for multidirectional waves. In: Proc. IAHR Seminar Multidirectional Waves and Their Interaction with Structures. 27th IAHR Congress. San Francisco.

Gobbi, M.F., Kirby, J.T., Wei, G., 2000. A fully nonlinear Boussinesq model for surface waves. Part 2. Extension to $O(kh)^4$. J. Fluid Mech. 405, 182–210. https://doi.org/10.1017/S0022112099007247.

Grilli, S.T., Horrillo, J., 1997. Numerical generation and absorption of fully nonlinear periodic waves. J. Eng. Mech. 123, 1060–1069. https://doi.org/10.1061/(ASCE)0733-9399(1997)123:10(1060).

Grilli, S.T., Vogelmann, S., Watts, P., 2002. Development of a 3D numerical wave tank for modeling tsunami generation by underwater landslides. Eng. Anal. Bound. Elem. 26, 301–313. https://doi.org/10.1016/S0955-7997(01)00113-8.

Gruwez, V., Altomare, C., Suzuki, T., Streicher, M., Cappietti, L., Kortenhaus, A., Troch, P., 2020. A CFD Inter-model Comparison for Wave Interactions with Sea Dikes on Shallow Foreshores (in press).

Ha, T., Lin, P., Cho, Y.S., 2013. Generation of 3D regular and irregular waves using Navier-Stokes equations model with an internal wave maker. Coast. Eng. 76, 55–67. https://doi.org/10.1016/j.coastaleng.2013.01.013.

Higdon, B.R.L., 1987. Numerical absorbing boundary conditions for the wave equation. Author (s): Robert L Higdon Source : Mathematics of Computation , Jul ., 1987 49 (179), 65–90 (Jul ., 1987) Published by : American Mathematical Society Stable URL : htt 49, 65–90.

Higuera, P., Lara, J.L., Losada, I.J., 2013a. Simulating coastal engineering processes with OpenFOAM®. Coast. Eng. 71, 119–134. https://doi.org/10.1016/j.coastaleng.2012.06.002.

Higuera, P., Lara, J.L., Losada, I.J., 2013b. Realistic wave generation and active wave absorption for Navier–Stokes models. Coast. Eng. 71, 102–118. https://doi.org/10.1016/j.coastaleng.2012.07.002.

Higuera, P., Losada, I.J., Lara, J.L., 2015. Three-dimensional numerical wave generation with moving boundaries. Coast. Eng. 101, 35–47. https://doi.org/10.1016/j.coastaleng.2015.04.003.

Jacobsen, N.G., Fuhrman, D.R., Fredsøe, J., 2012. A wave generation toolbox for the open-source CFD library: OpenFoam®. Int. J. Numer. Methods Fluid. 70, 1073–1088. https://doi.org/10.1002/fld.2726.

Kirby, J.T., 2016. Boussinesq models and their application to coastal processes across a wide range of scales. J. Waterw. Port, Coast. Ocean Eng. 142, 1–29. https://doi.org/10.1061/(ASCE)WW.1943-5460.0000350.

Larsen, J., Dancy, H., 1983. Open boundaries in short wave simulations–A new approach. Coast. Eng. 7, 285–297. https://doi.org/10.1016/0378-3839(83)90022-4.

Lee, C., Cho, Y.S., Yum, K., 2001. Internal generation of waves for extended Boussinesq equations. Coast. Eng. 42, 155–162. https://doi.org/10.1016/S0378-3839(00)00056-9.

Lin, P., Liu, P.L.F., 1998. A numerical study of breaking waves in the surf zone. J. Fluid Mech. 359, 239–264. https://doi.org/10.1017/S002211209700846X.

Lynett, P.J., Liu, P.L.F., 2004. Linear analysis of the multi-layer model. Coast. Eng. 51, 439–454. https://doi.org/10.1016/j.coastaleng.2004.05.004.

Lynett, P.J., Liu, P.L.F., 2002. A two-dimensional, depth-integrated model for internal wave propagation over variable bathymetry. Wave Motion 36, 221–240. https://doi.org/10.1016/S0165-2125(01)00115-9.

Ma, G., Shi, F., Kirby, J.T., 2012. Shock-capturing non-hydrostatic model for fully dispersive surface wave processes. Ocean Model. 43–44, 22–35. https://doi.org/10.1016/j.ocemod.2011.12.002.

Mayer, S., Garapon, A., Sørensen, L.S., 1998. A fractional step method for unsteady free-surface flow with applications to non-linear wave dynamics. Int. J. Numer. Methods Fluid. 28, 293–315. https://doi.org/10.1002/(SICI)1097-0363(19980815)28:2<293::AID-FLD719>3.0.CO;2-1.

Nicolae Lerma, A., Pedreros, R., Robinet, A., Sénéchal, N., 2017. Simulating wave setup and runup during storm conditions on a complex barred beach. Coast. Eng. 123, 29–41. https://doi.org/10.1016/j.coastaleng.2017.01.011.

Orszaghova, J., Borthwick, A.G.L., Taylor, P.H., 2012. From the paddle to the beach - a Boussinesq shallow water numerical wave tank based on Madsen and Sørensen's equations. J. Comput. Phys. 231, 328–344. https://doi.org/10.1016/j.jcp.2011.08.028.

Rijnsdorp, D.P., Hansen, J.E., Lowe, R.J., 2018. Simulating the wave-induced response of a submerged wave-energy converter using a non-hydrostatic wave-flow model. Coast. Eng. 140, 189–204. https://doi.org/10.1016/j.coastaleng.2018.07.004.

Rijnsdorp, D.P., Ruessink, G., Zijlema, M., 2015. Infragravity-wave dynamics in a barred coastal region, a numerical study. J. Geophys. Res. Ocean. 120, 4068–4089. https://doi.org/10.1002/2014JC010450.

Rijnsdorp, D.P., Smit, P.B., Zijlema, M., 2014. Non-hydrostatic modelling of infragravity waves under laboratory conditions. Coast. Eng. 85, 30–42. https://doi.org/10.1016/j.coastaleng.2013.11.011.

Sand, S.E., Mynett, A.E., 1987. Directional wave generation and analysis. In: IAHR Seminar on Wave Analysis and Generation in Laboratory Basins. Lausanne, Switzerland, pp. 363–376.

Schäffer, H.A., Sørensen, O.R., 2006. On the internal wave generation in Boussinesq and mild-slope equations. Coast. Eng. 53, 319–323. https://doi.org/10.1016/j.coastaleng.2005.10.022.

Shi, F., Kirby, J.T., Harris, J.C., Geiman, J.D., Grilli, S.T., 2012. A high-order adaptive time-stepping TVD solver for Boussinesq modeling of breaking waves and coastal inundation. Ocean Model. 43–44, 36–51. https://doi.org/10.1016/j.ocemod.2011.12.004.

Smit, P., Janssen, T., Holthuijsen, L., Smith, J., 2014. Non-hydrostatic modeling of surf zone wave dynamics. Coast. Eng. 83, 36–48. https://doi.org/10.1016/j.coastaleng.2013.09.005.

Smit, P., Zijlema, M., Stelling, G., 2013. Depth-induced wave breaking in a non-hydrostatic, near-shore wave model. Coast. Eng. 76, 1–16. https://doi.org/10.1016/j.coastaleng.2013.01.008.

Sørensen, O.R., Schäffer, H.A., Sørensen, L.S., 2004. Boussinesq-type modelling using an unstructured finite element technique. Coast. Eng. 50, 181–198. https://doi.org/10.1016/j.coastaleng.2003.10.005.

Stelling, G., Zijlema, M., 2003. An accurate and efficient finite-difference algorithm for non-hydrostatic free-surface flow with application to wave propagation. Int. J. Numer. Methods Fluid. 43, 1–23. https://doi.org/10.1002/fld.595.

Suzuki, T., Altomare, C., Veale, W., Verwaest, T., Trouw, K., Troch, P., Zijlema, M., 2017. Efficient and robust wave overtopping estimation for impermeable coastal structures in shallow foreshores using SWASH. Coast. Eng. 122, 108–123. https://doi.org/10.1016/j.coastaleng.2017.01.009.

Suzuki, T., Hu, Z., Kumada, K., Phan, L.K., Zijlema, M., 2019. Non-hydrostatic modeling of drag, inertia and porous effects in wave propagation over dense vegetation fields. Coast. Eng. 149, 49–64. https://doi.org/10.1016/j.coastaleng.2019.03.011.

Vasarmidis, P., Stratigaki, V., Suzuki, T., Zijlema, M., Troch, P., 2019b. Internal wave generation in a non-hydrostatic wave model. Water 11, 986. https://doi.org/10.3390/w11050986.

Vasarmidis, P., Stratigaki, V., Troch, P., 2019a. Accurate and fast generation of irregular short crested waves by using periodic boundaries in a mild-slope wave model. Energies 12, 785. https://doi.org/10.3390/en12050785.

Vincent, C.L., Briggs, M.J., 1989. Refraction—diffraction of irregular waves over a mound. J. Waterw. Port, Coast. Ocean Eng. 115, 269–284. https://doi.org/10.1061/(ASCE)0733-950X(1989)115:2(269).

Wei, G., Kirby, J.T., 1995. Time-dependent numerical code for extended Boussinesq equations. J. Waterw. Port, Coast. Ocean Eng. 121, 251–261. https://doi.org/10.1061/(ASCE)0733-950X(1995)121:5(251).

Wei, G., Kirby, J.T., Sinha, A., 1999. Generation of waves in Boussinesq models using a source function method. Coast. Eng. 36, 271–299. https://doi.org/10.1016/S0378-3839(99)00009-5.

Wellens, P., Borsboom, M., 2020. A generating and absorbing boundary condition for dispersive waves in detailed simulations of free-surface flow interaction with marine structures. Comput. Fluids 200, 104387. https://doi.org/10.1016/j.compfluid.2019.104387.

Zijlema, M., Stelling, G., Smit, P., 2011. SWASH: an operational public domain code for simulating wave fields and rapidly varied flows in coastal waters. Coast. Eng. 58, 992–1012. https://doi.org/10.1016/j.coastaleng.2011.05.015.

Zijlema, M., Stelling, G.S., 2008. Efficient computation of surf zone waves using the nonlinear shallow water equations with non-hydrostatic pressure. Coast. Eng. 55, 780–790. https://doi.org/10.1016/j.coastaleng.2008.02.020.